Journal of CO2 Utilization 83 (2024) 102784

Contents lists available at ScienceDirect

Journal of CO2 Utilization

journal homepage: www.elsevier.com/locate/jcou

Tailoring the A and B site of Fe-based perovskites for high selectivity in the reverse water-gas shift reaction

Alex Martinez Martin [a,†], Shailza Saini [b,†], Dragos Neagu [c], Wenting Hu [a], Ian S. Metcalfe [a], Kalliopi Kousi [b,*]

[a] School of Engineering, Newcastle University, Merz Court, Newcastle upon Tyne NE1 7RU, United Kingdom
[b] School of Chemistry and Chemical Engineering, University of Surrey, GU2 7XH, United Kingdom
[c] Department of Chemical and Process Engineering, University of Strathclyde, Glasgow, United Kingdom

ARTICLE INFO

Keywords:
Reverse water-gas shift
CO_2 utilization
Exsolution
Fe-Ni alloys
Lanthanide perovskites
Thermochemical CO_2 reduction

ABSTRACT

The reverse water-gas shift reaction (rWGS) is of particular interest as it is the first step to producing high-added-value products from carbon dioxide (CO_2) and renewable hydrogen (H_2), such as synthetic fuels or other chemical building blocks (e.g. methanol) through a modified Fischer-Tropsch process. However, side reactions and material deactivation issues, depending on the conditions used, still make it challenging. Efforts have been put into developing and improving scalable catalysts that can deliver high selectivity while at the same time being able to avoid deactivation through high temperature sintering and/or carbon deposition. Here we design a set of perovskite ferrites specifically tailored to the hydrogenation of CO_2 via the reverse water-gas shift reaction. We tailor the oxygen vacancies, proven to play a major role in the process, by partially substituting the primary A-site element (Barium, Ba) with Praseodymium (Pr) and Samarium (Sm), and also dope the B-site with a small amount of Nickel (Ni). We also take advantage of the exsolution process and manage to produce highly selective Fe-Ni alloys that suppress the formation of any by-products, leading to up to 100% CO selectivity.

1. Introduction

Mitigation of continuous emissions of greenhouse gases (GHG) and achieving net-zero have become key points in the latest agendas of international summits [1,2]. Among all the GHG emissions and because of its significant contribution to global warming, carbon dioxide (CO_2) still arises as the main concern [3]. Using CO_2 as a precursor for chemicals production could be the key to transforming the energy and chemicals industrial sectors while at the same time reducing GHG emissions. Indeed CO_2 can be transformed into valuable fuels and chemicals for energy, food or pharmaceutical industries [4] via its hydrogenation reactions. In particular, the reverse water-gas shift reaction (rWGS, (1)) is interesting as it can be the first step to producing high-added-value products, such as synthetic fuels or other chemical building blocks, such as methanol [5].

$$CO_2 + H_2 \rightleftharpoons CO + H_2O \Delta H^0_{298} = 42.1 kJ/mol \quad (1)$$

However, the rWGS is an endothermic reaction governed by equilibrium constraints and side reactions, such as methane (CH_4) formation. The conversion of CO_2 strongly depends on reaction conditions and is favoured at high temperatures. At lower temperatures, selectivity becomes an issue, generating CH_4, which requires additional products separation. Regarding catalyst requirements, a balance between oxygen vacancies and metallic active sites (particles) on the surface of a catalyst [6] is of utmost importance. In particular, the concentration of surface oxygen vacancies seems to play a crucial role to achieve high CO selectivity. Surface oxygen vacancies promote the activation and adsorption of CO_2. These oxygen vacancies in turn promote C═O bond dissociation from CO_2 and CO formation [3] while lattice oxygens serve as H_2 activation sites [7,8],. In addition, the high temperatures needed in this process and the use of CO_2 as a reactant often result in catalyst deactivation by sintering and/or carbon deposition [3,9,10]. Efforts have been put into developing and improving scalable catalysts that are able to provide active sites both for H_2 and CO_2 activation towards the desired products while at the same time can avoid deactivation. Noble metal catalysts offer a partial solution [11,12], but their use tends to be

* Corresponding author.
E-mail address: k.kousi@surrey.ac.uk (K. Kousi).
† The first two authors contributed equally.

https://doi.org/10.1016/j.jcou.2024.102784
Received 29 February 2024; Received in revised form 18 April 2024; Accepted 21 April 2024
Available online 30 April 2024

avoided given their scarcity and high costs [13]. Most of the research has been focused on transition metals, with particular interest in Fe-based [14–16] and Cu-based [17–19] systems [3] which seem to be highly active but very prone to sintering. Other materials, such as Ni-based systems, while very active and more stable, tend to favour CH_4 formation [20–22].

Perovskites have been employed as catalysts in rWGS lately due to their high capability for oxygen vacancy formation, possibility of forming defects and doping of different metals [23,24]. Perovskites are also known for their ability to serve as nanoparticle exsolution matrixes. Over the last few years, exsolution has emerged as a new approach that allows overcoming some of the above-mentioned challenges and is recognised as an alternative method to generate highly stable and durable catalysts [25–29]. In exsolution, the desired active phase is segregated from an oxide lattice, usually under reducing conditions, in the form of metallic nanoparticles anchored at its surface. These nanoparticles are socketed and somewhat embedded within the structure [30]. This makes the nanoparticles less prone to sintering under reaction conditions and endows the material with thermal resistance and/or higher activity over extended periods of time [31,32]. Exsolution has also been found to be of particular interest to the rWGS, where high CO selectivity and sustained high reaction rates were reported [15,33,34]. Although these studies are promising and some have even attempted to provide mechanistic insights into the process when using exsolved nanoparticles, this research is still in an early stage and a lot more research is needed in this area.

Here we design a set of perovskites specifically tailored to the hydrogenation of CO_2 via the reverse water gas shift reaction. We tailor the oxygen vacancies, proven to play a major role in the process by substituting lanthanides on the A-site (Pr and Sm) and dope Ni on the B-site and attempt to understand the impact of surface oxygen vacancies in CO_2 hydrogenation which is essential for tailoring the design of oxide-based catalysts with precision. We also take advantage of the exsolution process to produce highly selective Fe-Ni alloys that suppress the formation of any by-products, leading to up to 100% desired product selectivity. We characterise these catalysts via different techniques including but not limited to synchrotron X-ray diffraction, Scanning Electron Microscopy, and Catalytic Testing and provide a comprehensive understanding of the role of these design principles in the catalytic rWGS.

2. Experimental

2.1. Materials synthesis

$Ln_{0.5}Ba_{0.5}Fe_{1-x}Ni_xO_3$ (Ln = Pr, Sm; and x = 0, 0.1) were prepared according to the modified solid-state method [35]. Precursors used were Pr_6O_{11} (> 99.99%, Alfa Aesar), Sm_2O_3 (> 99.9%, Alfa Aesar), $BaCO_3$ (> 99.95%, Alfa Aesar), $Fe(NO_3)_3{\cdot}9\,H_2O$ (> 98%, Aldrich), and $Ni(NO_3)_2{\cdot}6\,H_2O$ (> 99.9985%, Alfa Aesar). Oxide precursors were previously dried at 400 ºC for 3 h. The nitrates and oxide precursors were added to a beaker in appropriate stoichiometric ratios. 30 mg of polymeric dispersant (HYPERMER KD1-SO-(AP)) were subsequently added to the mixture. This powder mixture was sonicated and calcined at 1000 ºC for 12 h, followed by ball-milling. This homogeneous mixture of powders was then pressed into pellets and fired at 1400 ºC at 14 h. After sintering, materials were crushed and sieved to obtain particle size between 80 and 160 μm. Final compounds were $Pr_{0.5}Ba_{0.5}FeO_{3-\delta}$ (PBFO) $Pr_{0.5}Ba_{0.5}Fe_{0.9}Ni_{0.1}O_{3-\delta}$ (PBFNO), $Sm_{0.5}Ba_{0.5}FeO_{3-\delta}$ (SBFO) and $Sm_{0.5}Ba_{0.5}Fe_{0.9}Ni_{0.1}\,O_{3-\delta}$ (SBFNO).

The sintered powder was reduced under 100 mL/min of 5% H_2 balanced in argon for 10 h at 900 ºC, in order to promote the exsolution of nanoparticles. Catalysts resulting from these reductions are denoted as *r*-PBFO, *r*-PBFNO, *r*-SBFO and *r*-SBFNO.

The reduced catalysts were also reoxidised (reactivated) in air at 600ºC for 60 min and then reduced under 5% H_2 balanced in argon *in situ* for 30 min at 600 ºC. All the heating rates were set to 5 ºC/min. Catalysts undergone this pretreatment are denoted as *ra*-PBFO, *ra*-PBFNO, *ra*-SBFO and *ra*-SBFNO.

2.2. Catalysts characterisation

Crystal structures were obtained by X-Ray diffraction measurements taken at the European Synchrotron Radiation Facility (ESRF). Samples were powdered and scans were carried out at room temperature with a radiation of 38 keV (λ = 0.35428 Å). Powders were loaded in 0.5 mm capillaries and the 2θ range covered from 0 to 40º, with an average collection time of 10 min per capillary. Refinement of the structures was carried out using TOPAS Academic v7 using cubic and tetragonal space groups. Parameters refined were background, thermal displacement, atomic coordinates, unit cell values and peak shapes. The sum of the occupancy for atoms of the A and B sites, i.e. Pr^{3+} and Ba^{2+} or Sm^{3+} and Ba^{2+}, and Fe^{3+} and Ni^{2+}, were constrained to unity. The pseudo-cubic cell parameters were obtained by calculating a weighted average between the phases. The pseudo-cubic cell parameter, a_p (Å), was obtained with Eq. (2):

$$a_p = \sqrt[3]{\frac{V_{unitc\quad cell}}{n_{unit\quad cell}}} \tag{2}$$

being $V_{unit\ cell}$ the volume of the real cell calculated by refinement and $n_{unit\ cell}$ the number of perovskite units contained within it.

Absolute oxygen content was measured by iodometric titration, following the process previously described [36]. A three necked round bottom flask was filled with 50 mL HCl (3 M) and purged with Ar, to create an oxygen-free environment. Materials (20 – 50 mg) were dissolved under continuous stirring and the solution was vented to a second Erlenmeyer containing an excess of KI (3 g) dissolved in deionised H_2O. A titration is subsequently done using 0.02 M $Na_2S_2O_3$ with starch as indicator. Each titration was conducted three times to ensure robustness in the measurements.

The surface properties and microstructure of the reduced and reactivated samples were determined using the Thermo Fischer Apreo 2 Scanning Electron Microscope (SEM). The acquisition of images took place at a voltage of 2 kV, with magnification levels ranging from 10,000 to 50,000, at a working distance of 4 mm. The images were analysed using Image J software to determine the particle size of the exsolved particles.

XPS analyses were performed on a Thermo Fisher Scientific (East Grinstead, UK) K-Alpha+ spectrometer. XPS spectra were acquired using a monochromated Al Kα X-ray source (h□ = 1486.6 eV). An X-ray spot of ~400 μm radius was employed. Survey spectra were acquired employing a Pass Energy of 200 eV. High resolution, core level spectra for all elements were acquired with a Pass Energy of 50 eV. All high-resolution core level spectra were charge referenced against the C1s peak at 285 eV to correct for charging effects during acquisition. Quantitative surface chemical analyses were calculated from the high resolution, core level spectra following the removal of a non-linear (Shirley) background. The manufacturers Avantage software was used which incorporates the appropriate sensitivity factors and corrects for the electron energy analyser transmission function.

2.3. Catalytic tests

Approximately 0.25 g (1 mmol) of catalyst was placed on quartz wool in the middle of a vertical, fixed-bed reactor measuring 1 cm. The reactor was 30 cm long and 1 cm in inner diameter. Gas flow was fed from the top of the reactor and a K-type thermocouple was placed as close as possible to the catalytic bed to monitor the temperature.

An initial screening was conducted with varying feed composition (H_2:CO_2), ranging from 1:1–4:1. We decided to proceed with the ratio 2:1 in this work because optimal selectivity was obtained with this

composition. All activity tests presented in this paper were conducted at atmospheric pressure with a total flow rate of 50 mL / min giving a Weight Hourly Space Velocity (WHSV) 12 L / (g_{cat}·h) with H_2:CO_2 ratio of 2:1 balanced in N_2. The reaction temperature was varied between 400 and 750 °C in increments of 50 °C, holding at each temperature until stabilisation. Carbon balance was closed within 2% error for each test. An on-line gas analyser (ABB AO2020 Advanced Optima Process Gas Analyser) was employed to measure reactants and products concentrations. Eqs. (3)-(5) are utilized for measuring the catalysts performance are provided below:

$$CO_2 \quad conversion \quad (\%) = \frac{[CO_2]_{in} - [CO_2]_{out}}{[CO_2]_{in}} * 100 \tag{3}$$

$$CO \quad selectivity \quad (\%) = \frac{[CO_2]_{out}}{[CO_2]_{in} - [CO_2]_{out}} * 100 \tag{4}$$

$$CH_4 \quad selectivity \quad (\%) = \frac{[CO_4]_{out}}{[CO_2]_{in} - [CO_2]_{out}} * 100 \tag{5}$$

The outlet concentrations of CO_2, CO and CH_4 in the reactor are represented by $[CO_2]_{Out}$, $[CO]_{Out}$ and $[CH_4]_{Out}$, respectively, while the initial CO_2 concentration in the gas mixture is denoted as $[CO_2]_{in}$.

To compare with the thermodynamic limits of the rWGS reaction at various temperatures with the selected H_2:CO_2 ratio, the ChemCad software package from ChemStations was employed. The Soave-Redlich-Kwong equation of state was implemented in a Gibbs reactor, and the material flows were set to match those intended for the experimentation.

3. Results and discussion

3.1. Materials design principles

Perovskite oxides are generally described with an ABO_3 structure, where A-sites are generally occupied by a rare-earth metal or an alkaline-earth metal while B-sites are usually occupied by a transition metal. Here we designed and prepared four different perovskites. Lanthanides or rare-earth metals were used in the A-site given their proven resistance to high temperatures in catalytic processes [15,17] and their active role in providing oxygen vacancies for CO_2 activation [37]. Overall, the oxygen content of a perovskite is complicated to predict and strongly dependant on cation's nature and their ratio in A-site and B-site positions. To monitor this relationship, in this work, Pr^{3+} and Sm^{3+} (Fig. 1a) were selected as substitutions of Ba^{2+} on the A-site which was originally chosen as it is known to promote oxygen mobility [38]. The smaller size of Sm^{3+} relative to Pr^{3+} requires more energy to form the lanthanide-oxygen bond [39] and this could promote the catalysts with a larger number of initial oxygen vacancies. Fe^{3+} served as the main transition metal on the B-site, as it is one of the main active elements for rWGS [14]. The incorporation of Ni on the B-site (Fig. 2a) was chosen as the formation of FeNi alloys has been reported to result in enhanced conversions and/or products' selectivity in catalytic processes [40,41], and at the same time presence of Ni is known to result in enhanced exsolution (even of Fe) due to its higher segregation energy [42]. The lower charge of Ni^{2+} as compared to Fe^{3+} could also induce the perovskite with more oxygen vacancies due to the additional oxygen non-stoichiometry introduced.

3.2. Synthesising Fe-based perovskites tailored at the A and B site; crystal structure, oxygen content and microstructure

The calcined powders were sintered at 1400 °C and were scanned under synchrotron X-rays. The diffraction patterns of the as-synthesised catalysts (Fig. 1b) showed characteristic perovskite peaks and indicated the formation of high-purity perovskites. Cubic perovskite phases were identified (*Pm-3 m*) for PBFO and SBFO (see *hkl* indices in Fig. 1b). Rietveld refinement (Fig. 1c) showed no evidence of any other phase.

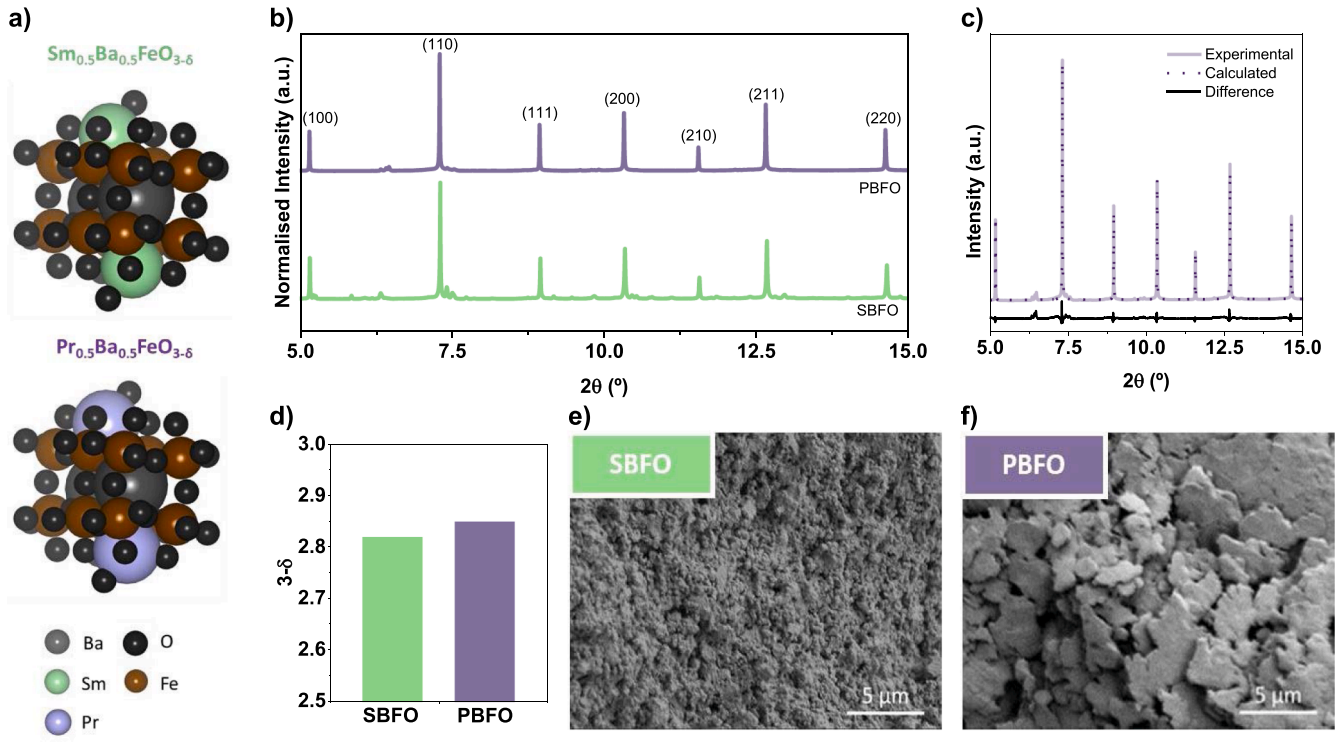

Fig. 1. Characterisation of A-site tailored ferrites. a) Schematic of the crystal structure $Sm_{0.5}Ba_{0.5}FeO_3$ (SBFO, top) and $Pr_{0.5}Ba_{0.5}FeO_3$ (PBFO, bottom). Visible difference in cationic size is represented by green (smaller, Sm) and purple (larger, Pr) cations. **b)** Synchrotron X-Ray patterns of the *as sintered* XRD patterns of the *as sintered* samples. hkl indexing corresponding to the perovskite phase on top of each peak. **c)** Example of Rietveld refinement of a single-phase perovskite. **d)** Oxygen non-stoichiometry of *as sintered* SBFO and PBFO, calculated by iodometric titration. Microstructure, by SEM images of *as sintered* SBFO, **e)** and PBFO, **f)**.

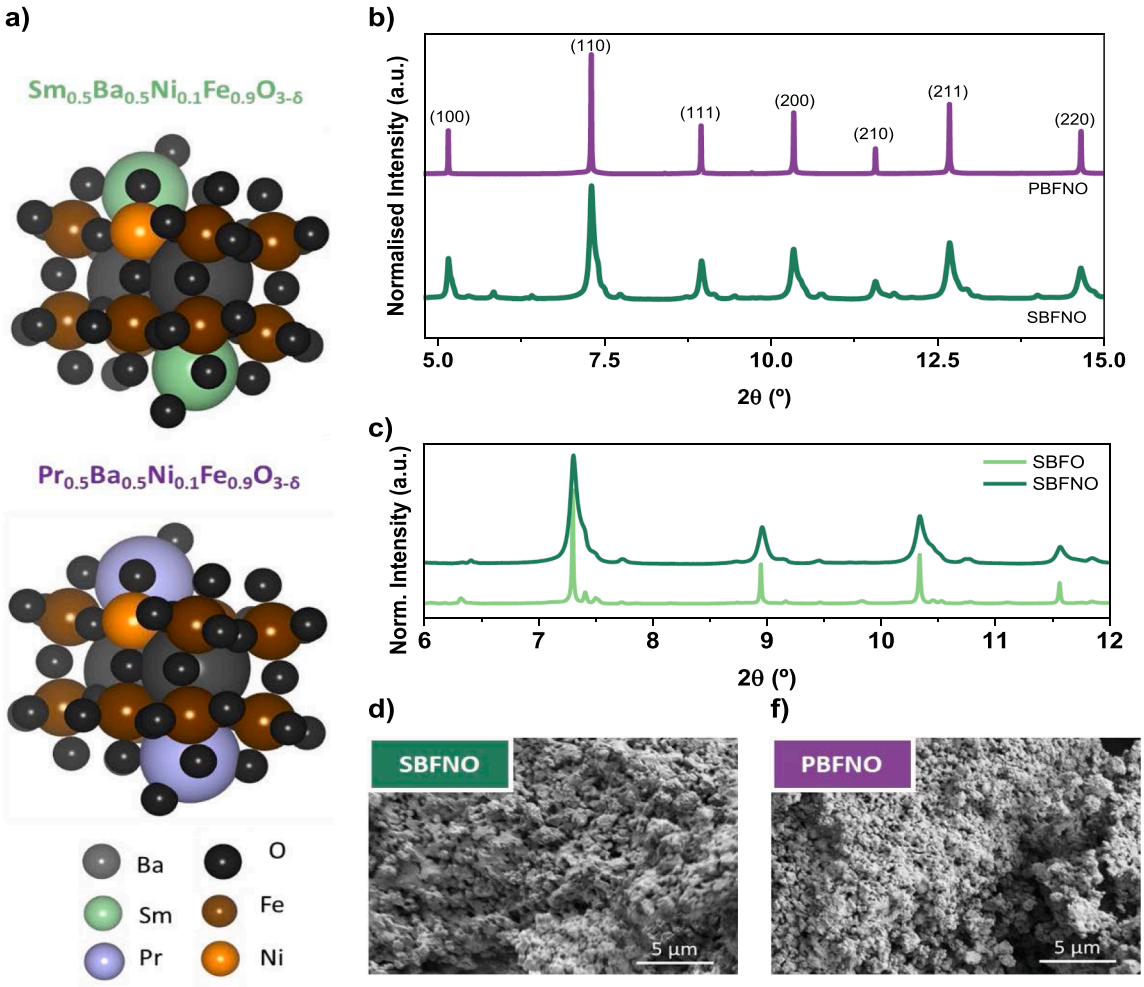

Fig. 2. Characterisation of B-site Ni-doped ferrites. a) Schematic depicting the substitution of both the A and B-site in a $BaFeO_{3-\delta}$. Visible difference in cationic size is represented by green (smaller, Sm) and purple (larger, Pr) cations. **b)** Synchrotron X-ray patterns of the *as sintered* samples. hkl indexing corresponding to the perovskite cubic phase on top of each peak. Superposition of SBFO and SBFNO for observation of peaks shape variation, **c)**. Catalysts microstructure, represented by SEM images of as-sintered SBFO, **d)** and PBFO, **e)**.

The effect of the larger size of Pr^{3+} as compared to Sm^{3+} and their effect on the oxygen content of the newly prepared materials are demonstrated by iodometric titration (Fig. 1d). As expected, the smaller size of Sm^{3+} (as compared to the Pr^{3+}) results in a less stable lanthanide-oxygen bond ($\Delta H_{f,Sm-O} = -135.6$ kJ / mol and $\Delta H_{f,\ Pr-O} = -147.7$ kJ / mol, respectively [39]), thereby creating more initial oxygen vacancies: 0.18 and 0.13 mol O / mol of catalyst, respectively. This implies that Sm-based catalysts could exhibit higher CO_2 activation capabilities. The catalysts microstructures demonstrated in Fig. 1e – f, as determined by scanning electron microscopy (SEM), were also very interesting. The PBFO seems to have a lot bigger grain size, which has a flake-like morphology as compared to its very porous, traditional-shaped, small grained SBFO analogue. The existence of smaller grains also reinforces the assumption that a SBFO could be an overall better sample as it could be more stable and have better surface area to exsolve upon.

Regarding the Ni doped samples, cubic perovskite phase was also identified (*Pm-3 m*) for the PBFNO while two symmetry groups coexisted however for SBFNO. This was observed by the lack of symmetry of the XRD peaks observed (see Fig. 1.b). Rietveld refinement confirmed the existence of a cubic (*Pm-3 m*, 69.0% of presence), a tetragonal (*P4/mmm*, 27.7% of presence) and an additional orthorhombic phase (*Pnma*, 3.3% of total contribution to the model). The cubic and tetragonal correspond to the SBFNO structure, being the tetragonal attributed to a higher oxygen non-stoichiometry. The latter, orthorhombic, corresponds to a $SmFeO_3$ secondary phase. The coexistence of three symmetry groups is also revealed by studying the pseudo-cubic cell parameter of SBFNO (3.696 Å) compared to its non Ni-doped analogue (SBFO, 3.929 Å). We attribute this variation to the distortion induced by both the smaller cationic radii of Sm^{3+} compared to Pr^{3+} (1.079 Å vs 1.179 Å, respectively) and the incorporation of Ni^{2+} within the B-site. These two factors combined entail a perturbation of the unit cell of the Sm-based catalyst resulting in the above phenomenon. It is also clear that Ni^{2+} has been successfully incorporated within the lattice since all the peaks are attributed to the main perovskite structure. The cationic radii values of Fe^{3+} and Ni^{2+} are still relatively close (0.645 Å and 0.69 Å, respectively), and the B-site substitution is minimal, resulting in a negligible distortion of the perovskite lattice, as the main cubic phase remains, even though a new tetragonal phase has been formed due to the insertion of Ni. Given the low influence of the new tetragonal phase (only 25% to the overall XRD spectrum), peaks display broadening at their base but no noticeable peak shifting is visible, as expected. Interestingly, while the SBFNO retains a microstructure very similar to its non-doped analogue, the microstructure of the PBFNO now resembles the one that is evident for the SBFO and SBFNO rather than that of its parent PBFO (Fig. 2.c, d).

3.3. Reducing the as synthesised materials; exsolution

In order to get metallic active sites and to potentially provoke exsolution the samples were subjected to a reduction in 5% H_2 (Ar

balance), at 900 ºC for 10 h [41,43]. SEM images of all the reduced samples are denoted as *r*-SBFO, *r*-PBFO, *r*-SBFNO, and *r*-PBFNO are shown in Fig. 3. The reduction of non-doped samples *r*-SBFO and *r*-PBFO at high-temperature results in the partial decomposition of the perovskite as seen by the SEM images. It seems like an uncontrolled segregation of large particles took place, which were most likely Fe based (particle size ~200 nm, Fig. 3a, c). Studies have shown that at high temperatures, Fe nanoparticles don't form the typical "socketed"

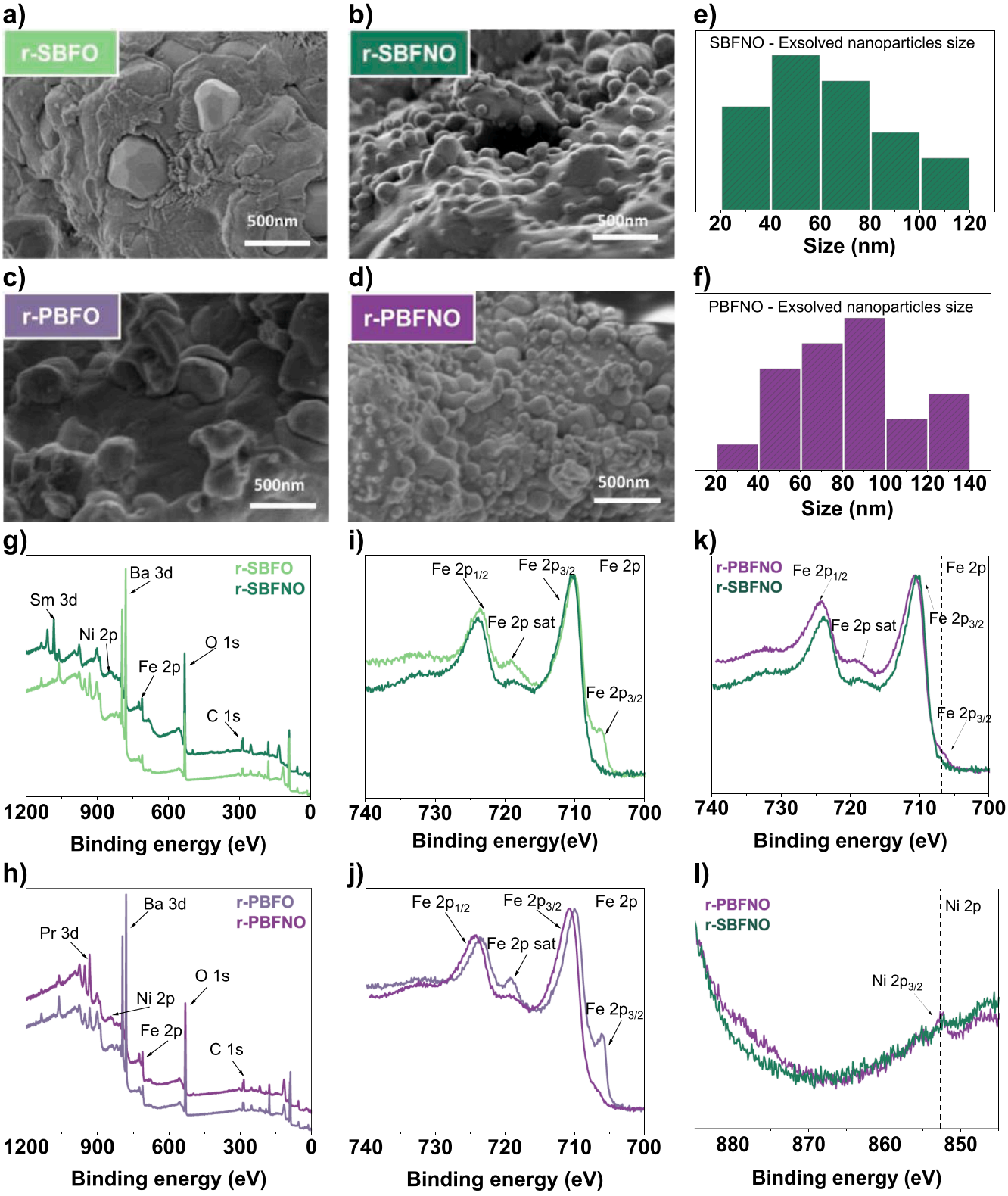

Fig. 3. Reducing the as-synthesised materials SEM images of catalysts after being reduced at 900ºC for 10 h. In order, *r*-SBFO, *r*-SBFNO, *r*-PBFO, *r*-PBFNO **a)-d)**. Particle distribution size for Ni-doped catalysts SBFNO, **e)**, PBNFO, **f)**. XPS survey spectra of *r*-SBFO and *r*-SBFNO **g),** *r*-PBFO and *r*-PBFNO catalysts. **i)** Fe 2p of Sm-based catalysts **j)** Fe 2p of Pr-based catalysts and Ni 2p, **k)** and **l)** for both reduced samples.

structure seen in exsolution. Instead, they undergo uncontrolled segregation, leading to the formation of larger Fe particles that detach from the host oxide [44,45]. The presence of iron particles is also confirmed by the XPS results given in Fig. 3.i-j.

On the other hand, partial substitution of Fe with Ni (10% at) in the B-site generates a more controlled segregation of nanoparticles. This is attributed to lower segregation energy caused by Ni-doping, as introducing easily reducible ions like Ni lowers the overall energy demand for cation diffusion, potentially paving the way for Fe to break free and form distinct metallic nanoparticles [43]. These particles are most likely Fe-Ni alloys, as Ni incorporation into the structure of ferrites has been demonstrated to result in both Fe and Ni undergoing exsolution, usually forming Fe-Ni alloy [40,46,47]. To further verify the nature of the in-situ exsolved nanoparticles as bimetallic Fe-Ni alloys, XPS was employed to analyse the materials' surface chemistry (Fig. 3.g-j). Based on analysing the XPS spectra, the peak located at the binding energy (BE) ~707 eV in Fig. 3.k is attributed to metallic iron (Fe^0) [48]. The peak position at ~709 eV and ~723 eV represents a doublet of Fe $2p_{3/2}$ and $2p_{1/2}$ orbital and the precise positioning of the satellite peaks associated with these Fe peaks is highly sensitive to oxidation states. The satellite peak of Fe $2p_{3/2}$ suggests a Fe^{3+} oxidation state for the iron in the materials [49]. The higher peak of the Fe $2p_{3/2}$ as compared to the Fe $2p_{1/2}$ peak arises due to spin-orbit coupling. XPS also confirmed the presence of Ni (see peak at ~852.6 eV Fig. 3j), corresponding to the Ni $2p_{3/2}$ orbital of metallic Ni [50]. However, the peak intensity is relatively low due to the limited concentration of the dopant and the even lower % of Ni exsolving overall. Interestingly, a slight shift in these BE was observed as compared to the non-Ni doped samples as seen in Fig. 3i-j. Specifically, for the Ni-doped samples, a shift of the whole Fe spectra towards higher values is observed. This suggests a potential electronic interaction between these neighbouring atoms involving a partial charge transfer (Fe^{3+} → Ni^{2+}). This bimetallic interaction could imply the formation of the Fe-Ni alloy nanoparticles [47,51]. The Fe-Ni alloy nanoparticle size distribution for both the samples is quite wide, ranging from 40 to 80 nm for the Sm sample and 40–100 nm for the Pr sample (Fig. 3e and f). This behaviour is characteristic of the reversible type of exsolution that happens when A-site stochiometric samples are used [35].

3.4. Catalytic activity of the new catalysts in rWGS

The CO_2 conversion with temperature in the rWGS reaction is illustrated in Fig. 4. The equilibrium values are also included in these figures for comparison. As expected, CO_2 conversion increases with temperature, in all catalysts. The most active sample seems to be *r*-SBFO, mainly around the 550–700ºC temperature range. It reached maximum CO_2 conversion of 56% at 750 ºC and was very close to the thermodynamic equilibrium through the temperature range > 600 ºC, Fig. 4a. Surprisingly, Ni-doped catalysts do not display higher reactivity than their non-doped analogues. Catalysts' activity trend is *r*-SBFO > *r*-PBFO > *r*-PBFNO > *r*-SBFNO, indicating that non-doped samples are actually more active than the Ni-doped samples. Generally, Ni samples were expected to be more active overall in converting CO_2 since Ni-based samples due to additional vacancy formation during reduction could help activate CO_2, albeit probably to CH_4 not CO [15]. Surprisingly, this is not what our results indicate.

Previous studies have demonstrated that catalysts with reducible supports are more prone to follow a Mars-van Krevelen (MvK)-type redox mechanism [6]. In this mechanism, CO_2 requires oxygen vacancies to be activated and in turn it provides the lattice with labile oxygen atoms, while H_2 needs to be split by a metal (Fe in this case) and subsequently react with the provided oxygen to form H_2O, which is also thought to be the rate-limiting step of the overall rWGS process [6,15]. Thus the presence of oxygen vacancies is necessary to reduce CO_2 whereas the exsolved metallic active sites and the lattice oxygen are needed to promote the dissociative mechanism of H_2 oxidation [6]. The enhanced activity of *r*-SBFO compared to *r*-PBFO is attributed to the difference between the two A-site metals, Sm and Pr, since the Sm-based catalysts are expected to possess a larger amount of oxygen vacancies than the Pr-based analogues [39], as also described above. Taking this into consideration it is possible that while the exsolution of Ni does provide the sample with the active sites and the vacancies needed, it also depletes the materials of lattice oxygen hence they appear to be less active [6]. Indeed, both Ni-doped perovskites followed this trend.

Regarding selectivity, at low temperatures (~400 ºC-500 ºC), the selectivity of the Ni-doped catalysts (Fig. 4c, d) to CO increases.

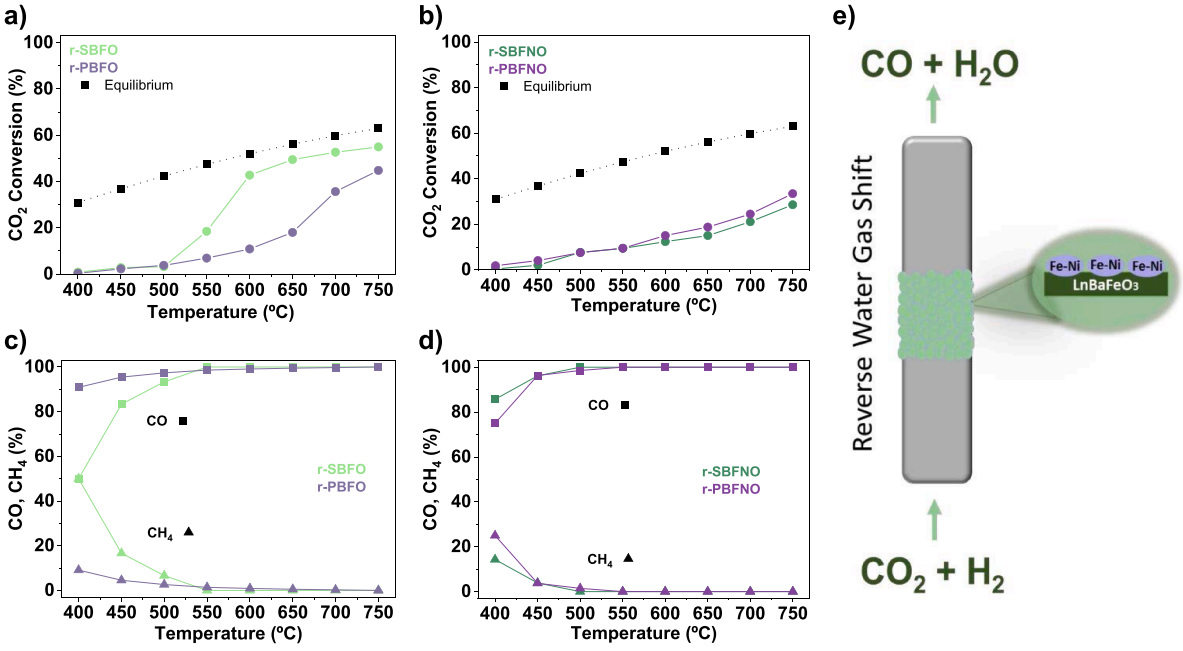

Fig. 4. Employing the newly prepared ferrites in rWGS. CO_2 conversion with temperature for reduced SBFO and PBFO **a)** and reduced Ni-doped counterparts **b)**. Both graphs display an equilibrium curve for the tested temperatures. Products selectivity at different temperature for reduced SBFO and PBFO **c)** and reduced Ni-doped counterparts **d)**. CO selectivity is represented with square (■) and CH_4 selectivity is represented with triangle (▲), **e)** Schematic representation of the concept presented here.

Specifically, a ~25% increase is demonstrated for the *r*-SBFNO (75% vs 50% for the *r*-SBFO), minimising the formation of CH_4 which is generally favoured at these temperatures and even reaches 100% selectivity to CO at higher temperatures. Similarly to Sm-based catalysts, the presence of Ni also increased the selectivity for Pr-based materials. The high selectivity towards CO over CH_4 is indeed expected to be a result of the Fe-Ni alloy formation as previously reported in the literature [52].

3.5. Replenishing the lattice oxygen

To test the potential connection between the lattice oxygen depletion during exsolution and the activity of the Ni-doped samples, the reduced catalysts were subjected to re-oxidation (600 °C for 30 min) in order to replenish the lattice oxygen. Upon oxidation, the material underwent a subsequent reduction step at 600 °C for 30 min. This specific temperature and duration were chosen to prevent the complete removal of the newly replenished lattice oxygen but solely reduce the surface active species/particles as reduction is known to be much slower than oxidation. These new samples are now denoted as *ra*-PBFO, *ra*-PBFNO, *ra*-SBFO and *ra*-SBFNO. Fig. 5a and b show the catalytic activity of the reactivated perovskites, with CO_2 conversion as a function of temperature. It is worth noting that the 'reduced' data in Fig. 5 is the same data that is shown in Fig. 4. In this case, *ra*-SBFNO exhibited the highest activity (closely followed by PBFNO especially at lower temperatures), doubling its conversion from 28% to 56% (Fig. 5b), almost reaching equilibrium values. *ra*-PBFNO increased CO_2 conversion activity by ~10% (42% vs 32% on *r*-PBFNO). The increasing trend in conversion highlights the positive effect our pretreatment. Remarkably, upon reactivation, all catalysts showcased complete suppression of methane formation and achieved 100% selectivity (Fig. 5c, d, open symbols).

On the other hand, this pre-treatment led to the deactivation of the *ra*-SBFO (Fig. 5a), with maximum conversion dropping to 19%. This decrease in activity is probably due to the practical destruction of the SBFO microstructure after reoxidation, as depicted in Fig. 6a. Despite the fact that SBFNO showed the highest catalytic activity SEM images revealed changes in the microstructure (Fig. 6b) that imply partial decomposition as this is similar to A-site segregation reported in the literature [53]. The reactivation process seems to not have impacted negatively the Pr based materials as the conversion of the *ra*-PBFO was almost identical as before (Fig. 6c) and increased for the *ra*-PBFNO (Fig. 6d) for, which also demonstrated a similar micro/nanostructure as before reactivation.

4. Conclusions

We have designed a set of four different tailored and exsolved perovskites for the catalytic rWGS. We demonstrate that the substitution of the A-site and doping B-site as well as the concentration of oxygen vacancies are important design principles to consider when designing a material for the conversion of CO_2 to CO. Our results show that A-site

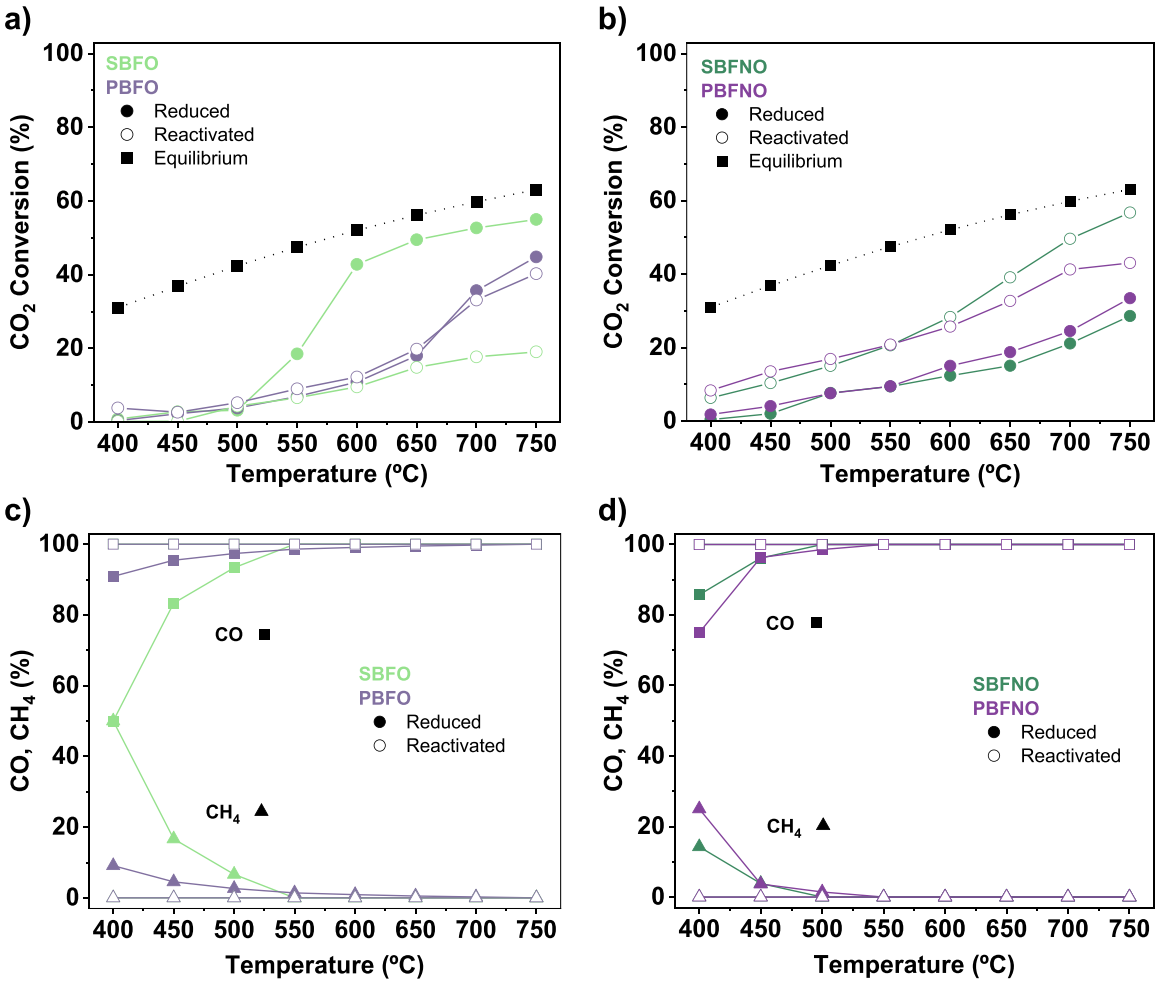

Fig. 5. Catalytic testing of the reactivated materials. CO_2 conversion with temperature for reduced (●) and reactivated (○) SBFO and PBFO **a)** and Ni-doped counterparts **b)**. Both graphs display an equilibrium curve for the tested temperatures. Products selectivity at different temperatures for reduced (●) and reactivated (○) SBFO and PBFO **c)** and reduced Ni-doped counterparts **d)**. CO selectivity is represented with a square (■) and CH_4 selectivity is represented with a triangle (▲). Selectivity values are identical for the reactivated samples hence they might not be visible in the graphs.

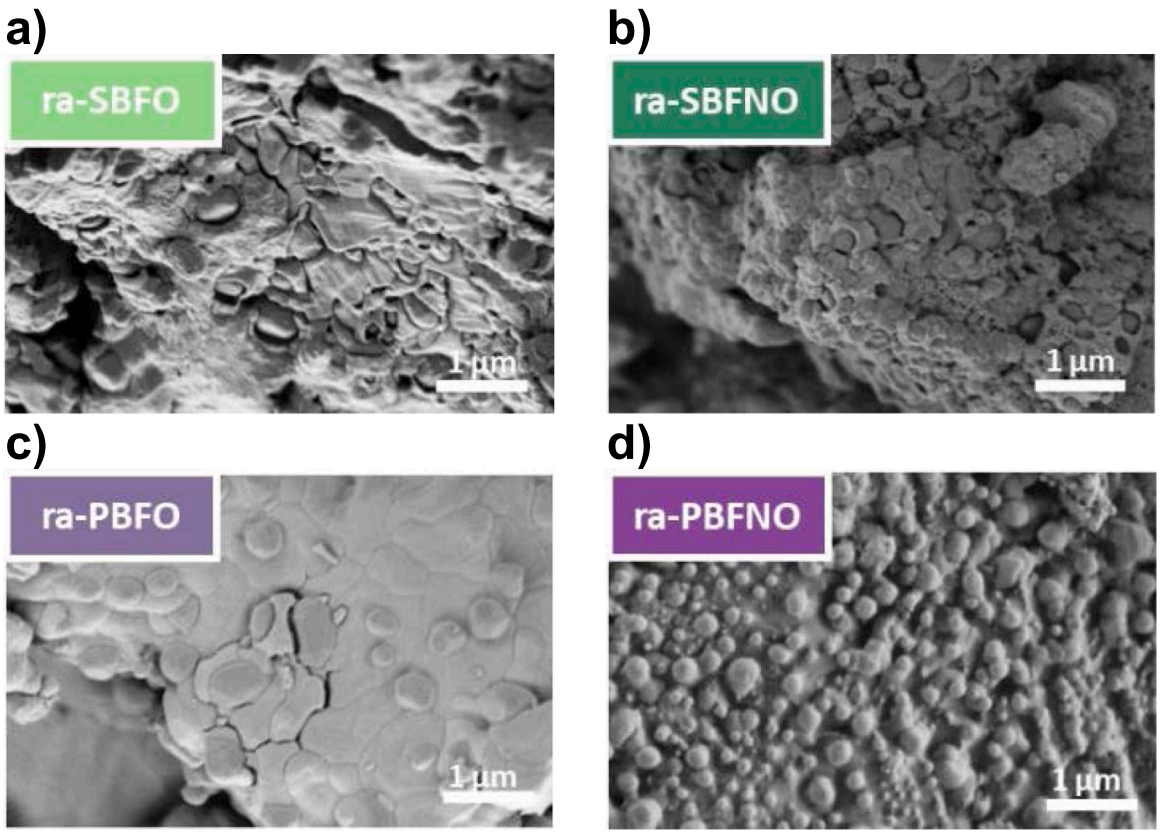

Fig. 6. Characterisation of reactivated materials SEM images of catalysts after being reduced at 600ºC for 1 h after undergoing exsolution at 900ºC for 10 h, subsequent reoxidation at 600ºC for 30 min. In order: ra-SBFO, ra-SBFNO, ra-PBFO, ra-PBFNO, **a-d)**.

doping with Pr appears to produce more stable catalysts when compared to Sm doped ones, even though the latter tends to be slightly more active. We also show that the existence of lattice oxygen is crucial for this process and has to be taken into consideration for efficient future material design. For the best catalytic activity, a balance between H_2 activation and CO_2 dissociation should be tailored by the oxygen vacancy concentration. We demonstrate more oxygen vacancies does not always result in better activity. Lastly, the incorporation of a small quantity of Ni on the B-site combined with exsolution results in very high selectivity, with no methane formation, even at low temperatures where methanation conditions are favourable due to the production of Fe-Ni alloys. Although there is still room for improvement for our catalysts regarding their stability and low temperature activity, our results provide a new insight of the significance of oxygen vacancies in CO_2 hydrogenation. These findings imply the potential of such materials for low-temperature RWGS processes that include the production of liquid fuels either downstream or in combination in the same reactors.

Author agreement statement

We the undersigned declare that this manuscript is original, has not been published before and is not currently being considered for publication elsewhere. We confirm that the manuscript has been read and approved by all named authors and that there are no other persons who satisfied the criteria for authorship but are not listed. We further confirm that the order of authors listed in the manuscript has been approved by all of us. We understand that the Corresponding Author is the sole contact for the Editorial process. He/she is responsible for communicating with the other authors about progress, submissions of revisions and final approval of proofs.

CRediT authorship contribution statement

Ian S. Metcalfe: Writing – review & editing, Supervision, Resources, Methodology, Funding acquisition. **Wenting Hu:** Writing – review & editing, Supervision, Methodology. **Alex Martinez-Martin:** Writing – original draft, Methodology, Investigation, Formal analysis, Data curation. **Dragos Neagu:** Writing – review & editing, Supervision, Methodology. **Shailza Saini:** Writing – original draft, Methodology, Investigation, Formal analysis, Data curation. **Kalliopi Kousi:** Writing – review & editing, Supervision, Resources, Project administration, Methodology, Funding acquisition, Conceptualization.

Declaration of Competing Interest

The authors declare that they have no known competing financial interests or personal relationships that could have appeared to influence the work reported in this paper.

Data availability

Supporting research data for this article may be accessed at 10.15126/surreydata.900994.

Acknowledgements

The research leading to these results was funded by the School of Chemistry and Chemical Engineering (Chemical and Process Engineering), by the Royal Society RGS\R2\222062, and the Engineering and Physical Science Research Council EP/Y015487/1. Ian S. Metcalfe acknowledges funding from the Royal Academy of Engineering through a Chair in Emerging Technologies Award entitled “Engineering Chemical Reactor Technologies for a Low-Carbon Energy Future” (Grant

CiET1819\2\57). We acknowledge the European Synchrotron Radiation Facility (ESRF) for provision of synchrotron radiation facilities, and we would like to thank Dr Catherine Dejoie for assistance and support in using beamline ID22. We would like to thank Prof. John Evans for his assistance during the time in the ESRF by developing software scripts that allowed for analysis of the XRD data.

References

[1] IPCC, Summary for Policymakers Sixth Assessment Report (WG3), 2022. ⟨https://www.ipcc.ch/report/ar6/wg2/⟩.
[2] U.N.C. Change, COP28 Agreement Signals “Beginning of the End” of the Fossil Fuel Era, (2023). ⟨https://unfccc.int/news/cop28-agreement-signals-beginning-of-the-end-of-the-fossil-fuel-era⟩.
[3] M. González-Castaño, B. Dorneanu, H. Arellano-García, The reverse water gas shift reaction: a process systems engineering perspective, React. Chem. Eng. 6 (2021) 954–976, https://doi.org/10.1039/d0re00478b.
[4] M. Mikkelsen, M. Jørgensen, F.C. Krebs, The teraton challenge. A review of fixation and transformation of carbon dioxide, Energy Environ. Sci. 3 (2010) 43–81, https://doi.org/10.1039/b912904a.
[5] C. Wu, D. Cheng, M. Wang, D. Ma, Understanding and application of strong metal-support interactions in conversion of CO_2 to methanol: a review, Energy Fuels 35 (2021) 19012–19023, https://doi.org/10.1021/acs.energyfuels.1c02440.
[6] A.K. Opitz, A. Nenning, V. Vonk, S. Volkov, F. Bertram, H. Summerer, S. Schwarz, A. Steiger-Thirsfeld, J. Bernardi, A. Stierle, J. Fleig, Understanding electrochemical switchability of perovskite-type exsolution catalysts, Nat. Commun. 2020 111 11 (1) (2020) 10, https://doi.org/10.1038/s41467-020-18563-w.
[7] G. Vilé, S. Colussi, F. Krumeich, A. Trovarelli, J. Pérez-Ramírez, Opposite face sensitivity of CeO2 in hydrogenation and oxidation catalysis, Angew. Chem. Int Ed. 53 (2014) 12069–12072, https://doi.org/10.1002/ANIE.201406637.
[8] G. Vilé, B. Bridier, J. Wichert, J. Pérez-Ramírez, Ceria in hydrogenation catalysis: High selectivity in the conversion of alkynes to olefins, Angew. Chem. - Int Ed. 51 (2012) 8620–8623, https://doi.org/10.1002/anie.201203675.
[9] E. Pahija, C. Panaritis, S. Gusarov, J. Shadbahr, F. Bensebaa, G. Patience, D. C. Boffito, Experimental and computational synergistic design of Cu and Fe catalysts for the reverse water-gas shift: a review, ACS Catal. 12 (2022) 6887–6905, https://doi.org/10.1021/acscatal.2c01099.
[10] J.A. Loiland, M.J. Wulfers, N.S. Marinkovic, R.F. Lobo, Fe/γ-Al_2O_3 and Fe-K/γ-Al_2O_3 as reverse water-gas shift catalysts, Catal. Sci. Technol. 6 (2016) 5267–5279, https://doi.org/10.1039/c5cy02111a.
[11] K. Oshima, T. Shinagawa, Y. Nogami, R. Manabe, S. Ogo, Y. Sekine, Low temperature catalytic reverse water gas shift reaction assisted by an electric field, Catal. Today 232 (2014) 27–32, https://doi.org/10.1016/j.cattod.2013.11.035.
[12] S. Kattel, B. Yan, J.G. Chen, P. Liu, CO2 hydrogenation on Pt, Pt/SiO2 and Pt/TiO2: importance of synergy between Pt and oxide support, J. Catal. 343 (2016) 115–126, https://doi.org/10.1016/j.jcat.2015.12.019.
[13] L.H. Vieira, L.F. Rasteiro, C.S. Santana, G.L. Catuzo, A.H.M. da Silva, J.M. Assaf, E. M. Assaf, Noble metals in recent developments of heterogeneous catalysts for CO_2 conversion processes, ChemCatChem 15 (2023), https://doi.org/10.1002/cctc.202300493.
[14] L. Pastor-Pérez, M. Shah, E. Le Saché, T.R. Reina, Improving Fe/Al2O_3 catalysts for the reverse water-gas shift reaction: on the effect of Cs as activity/selectivity promoter, Page 608. 8 (2018), Catal Vol 8 (2018) 608, https://doi.org/10.3390/CATAL8120608.
[15] L. Lindenthal, J. Popovic, R. Rameshan, J. Huber, F. Schrenk, T. Ruh, A. Nenning, S. Löffler, A.K. Opitz, C. Rameshan, Novel perovskite catalysts for CO_2 utilization - Exsolution enhanced reverse water-gas shift activity, Appl. Catal. B Environ. 292 (2021) 120183, https://doi.org/10.1016/J.APCATB.2021.120183.
[16] S. Sengupta, A. Jha, P. Shende, R. Maskara, A.K. Das, Catalytic performance of Co and Ni doped Fe-based catalysts for the hydrogenation of CO2 to CO via reverse water-gas shift reaction, J. Environ. Chem. Eng. 7 (2019) 102911, https://doi.org/10.1016/J.JECE.2019.102911.
[17] H.X. Liu, S.Q. Li, W.W. Wang, W.Z. Yu, W.J. Zhang, C. Ma, C.J. Jia, Partially sintered copper-ceria as excellent catalyst for the high-temperature reverse water gas shift reaction, Nat. Commun. 13 (2022) 1–11, https://doi.org/10.1038/s41467-022-28476-5.
[18] X. Zhang, X. Zhu, L. Lin, S. Yao, M. Zhang, X. Liu, X. Wang, Y.W. Li, C. Shi, D. Ma, Highly dispersed copper over β-Mo_2C as an efficient and stable catalyst for the reverse water gas shift (RWGS) reaction, ACS Catal. 7 (2017) 912–918, https://doi.org/10.1021/acscatal.6b02991.
[19] D.L. Jurković, A. Pohar, V.D.B.C. Dasireddy, B. Likozar, Effect of copper-based catalyst support on reverse water-gas shift reaction (RWGS) activity for CO_2 reduction, Chem. Eng. Technol. 40 (2017) 973–980, https://doi.org/10.1002/ceat.201600594.
[20] L. Wang, S. Zhang, Y. Liu, Reverse water gas shift reaction over Co-precipitated Ni-CeO2 catalysts, J. Rare Earths 26 (2008) 66–70, https://doi.org/10.1016/S1002-0721(08)60039-3.
[21] L. Wang, H. Liu, Y. Liu, Y. Chen, S. Yang, Effect of precipitants on Ni-CeO_2 catalysts prepared by a co-precipitation method for the reverse water-gas shift reaction, J. Rare Earths 31 (2013) 969–974, https://doi.org/10.1016/S1002-0721(13)60014-9.
[22] F.M. Sun, C.F. Yan, Z. Da Wang, C.Q. Guo, S.L. Huang, Ni/Ce-Zr-O catalyst for high CO_2 conversion during reverse water gas shift reaction (RWGS), Int J. Hydrog. Energy 40 (2015) 15985–15993, https://doi.org/10.1016/j.ijhydene.2015.10.004.
[23] T.H. Shin, Y. Okamoto, S. Ida, T. Ishihara, Self-recovery of Pd nanoparticles that were dispersed over La(Sr)Fe(Mn)O3 for intelligent oxide anodes of solid-oxide fuel cells, 11695–1102, Chem. - A Eur. J. 18 (2012), https://doi.org/10.1002/chem.201200536.
[24] L. Lindenthal, R. Rameshan, H. Summerer, T. Ruh, J. Popovic, A. Nenning, S. Löffler, A.K. Opitz, P. Blaha, C. Rameshan, Modifying the surface structure of perovskite-based catalysts by nanoparticle exsolution, Catalysts 10 (2020) 1–14, https://doi.org/10.3390/catal10030268.
[25] K. Kousi, C. Tang, I.S. Metcalfe, D. Neagu, K. Kousi, S. Metcalfe, C. Tang, D. Neagu, Emergence and future of exsolved materials, Small 17 (2021) 2006479, https://doi.org/10.1002/SMLL.202006479.
[26] O. Kwon, S. Joo, S. Choi, S. Sengodan, G. Kim, Review on exsolution and its driving forces in perovskites, JPhys Energy 2 (2020), https://doi.org/10.1088/2515-7655/ab8c1f.
[27] Q.A. Islam, S. Paydar, N. Akbar, B. Zhu, Y. Wu, Nanoparticle exsolution in perovskite oxide and its sustainable electrochemical energy systems, J. Power Sources 492 (2021) 229626, https://doi.org/10.1016/j.jpowsour.2021.229626.
[28] Z. Sun, C. Hao, S. Toan, R. Zhang, H. Li, Y. Wu, H. Liu, Z. Sun, Recent advances in exsolved perovskite oxide construction: exsolution theory, modulation, challenges, and prospects, J. Mater. Chem. A 11 (2023) 17961–17976, https://doi.org/10.1039/d3ta03292b.
[29] D. Neagu, J.T.S. Irvine, J. Wang, B. Yildiz, A.K. Opitz, J. Fleig, Y. Wang, J. Liu, L. Shen, F. Ciucci, B.A. Rosen, Y. Xiao, K. Xie, G. Yang, Z. Shao, Y. Zhang, J. Reinke, T.A. Schmauss, S.A. Barnett, R. Maring, V. Kyriakou, U. Mushtaq, M.N. Tsampas, Y. Kim, R. O’Hayre, A.J. Carrillo, T. Ruh, L. Lindenthal, F. Schrenk, C. Rameshan, E.I. Papaioannou, K. Kousi, I.S. Metcalfe, X. Xu, G. Liu, Roadmap on exsolution for energy applications, J. Phys. Energy 5 (2023) 031501, https://doi.org/10.1088/2515-7655/ACD146.
[30] K. Kousi, D. Neagu, L. Bekris, E.I. Papaioannou, I.S. Metcalfe, Endogenous nanoparticles strain perovskite host lattice providing oxygen capacity and driving oxygen exchange and CH 4 conversion to syngas, Angew. Chem. 132 (2020) 2531–2540, https://doi.org/10.1002/ange.201915140.
[31] S.K. Otto, K. Kousi, D. Neagu, L. Bekris, J. Janek, I.S. Metcalfe, Exsolved nickel nanoparticles acting as oxygen storage reservoirs and active sites for redox CH4 conversion, ACS Appl. Energy Mater. 2 (2019) 7288–7298, https://doi.org/10.1021/acsaem.9b01267.
[32] D. Zubenko, S. Singh, B.A. Rosen, Exsolution of Re-alloy catalysts with enhanced stability for methane dry reforming, Appl. Catal. B Environ. 209 (2017) 711–719, https://doi.org/10.1016/j.apcatb.2017.03.047.
[33] F. Orsini, D. Ferrero, S.F. Cannone, M. Santarelli, A. Felli, M. Boaro, C. de Leitenburg, A. Trovarelli, J. Llorca, G. Dimitrakopoulos, A.F. Ghoniem, Exsolution-enhanced reverse water-gas shift chemical looping activity of $Sr_2FeMo_{0.6}Ni_{0.4}O_{6-\delta}$ double perovskite, Chem. Eng. J. 475 (2023) 146083, https://doi.org/10.1016/j.cej.2023.146083.
[34] J. Zhou, Z. Zhu, Q. Li, Q. Zhang, Z. Liu, Q. Deng, Z. Zhou, C. Li, L. Fu, J. Zhou, H. Li, K. Wu, Fabrication of heterostructural FeNi3-loaded perovskite catalysts by rapid plasma for highly efficient photothermal reverse water gas shift reaction, Small 2307302 (2023) 1–10, https://doi.org/10.1002/smll.202307302.
[35] D. Neagu, G. Tsekouras, D.N. Miller, H. Ménard, J.T.S. Irvine, In situ growth of nanoparticles through control of non-stoichiometry, Nat. Chem. 5 (2013) 916–923, https://doi.org/10.1038/nchem.1773.
[36] M.D. Carvalho, L.P. Ferreira, M.T. Colomer, P. Gaczyński, M.M. Cruz, J. C. Waerenborgh, M. Godinho, Magnetic studies on $Sr_{0.8}Ce_{0.1}Fe_{0.7}Co_{0.3}O_{3-\delta}$ perovskite, Solid State Sci. 8 (2006) 444–449, https://doi.org/10.1016/j.solidstatesciences.2005.12.001.
[37] H. Ban, C. Li, K. Asami, K. Fujimoto, Influence of rare-earth elements (La, Ce, Nd and Pr) on the performance of Cu/Zn/Zr catalyst for CH_3OH synthesis from CO_2, Catal. Commun. 54 (2014) 50–54, https://doi.org/10.1016/J.CATCOM.2014.05.014.
[38] J. Song, D. Ning, H.J.M. Bouwmeester, Influence of alkaline-earth metal substitution on structure, electrical conductivity and oxygen transport properties of perovskite-type oxides La0.6A0.4FeO3−δ(A = Ca, Sr and Ba), Phys. Chem. Chem. Phys. 22 (2020) 11984–11995, https://doi.org/10.1039/d0cp00247j.
[39] N.E. Volkova, M.Y. Mychinko, I.B. Golovachev, A.E. Makarova, M.V. Bazueva, E. I. Zyaikin, L.Y. Gavrilova, V.A. Cherepanov, Structure and properties of layered perovskites $Ba_{1-x}Ln_xFe_{1-y}Co_yO_{3-\delta}$ (Ln = Pr, Sm, Gd), J. Alloy. Compd. 784 (2019) 1297–1302, https://doi.org/10.1016/J.JALLCOM.2018.12.391.
[40] Y.F. Sun, J.H. Li, L. Cui, B. Hua, S.H. Cui, J. Li, J.L. Luo, A-site-deficiency facilitated in situ growth of bimetallic Ni–Fe nano-alloys: a novel coking-tolerant fuel cell anode catalyst, Nanoscale 7 (2015) 11173–11181, https://doi.org/10.1039/C5NR02518D.
[41] D. Papargyriou, D.N. Miller, J.T.S. Irvine, Exsolution of Fe-Ni alloy nanoparticles from (La,Sr)(Cr,Fe,Ni)O_3 perovskites as potential oxygen transport membrane catalysts for methane reforming, J. Mater. Chem. A 7 (2019) 15812–15822, https://doi.org/10.1039/c9ta03711j.
[42] C. Tang, K. Kousi, D. Neagu, I.S. Metcalfe, Trends and prospects of bimetallic exsolution, Chem. - A Eur. J. 27 (2021) 6666–6675, https://doi.org/10.1002/chem.202004950.
[43] S. Ding, M. Li, W. Pang, B. Hua, N. Duan, Y.Q. Zhang, S.N. Zhang, Z. Jin, J.L. Luo, A-site deficient perovskite with nano-socketed Ni-Fe alloy particles as highly active and durable catalyst for high-temperature CO2 electrolysis, Electro Acta 335 (2020) 135683, https://doi.org/10.1016/J.ELECTACTA.2020.135683.

[44] S. Jo, Y. Han Kim, H. Jeong, C. ho Park, B.R. Won, H. Jeon, K. Taek Lee, J. ha Myung, Exsolution of phase-separated nanoparticles via trigger effect toward reversible solid oxide cell, Appl. Energy 323 (2022) 119615, https://doi.org/10.1016/j.apenergy.2022.119615.

[45] M. Santaya, C.E. Jiménez, M.D. Arce, E.A. Carbonio, L.M. Toscani, R. Garcia-Diez, A. Knop-Gericke, L.V. Mogni, M. Bär, H.E. Troiani, Exsolution versus particle segregation on (Ni,Co)-doped and undoped SrTi0.3Fe0.7O3-δ perovskites: differences and influence of the reduction path on the final system nanostructure, Int. J. Hydrog. Energy 48 (2023) 38842–38853, https://doi.org/10.1016/j.ijhydene.2023.06.203.

[46] Z. Du, H. Zhao, S. Yi, Q. Xia, Y. Gong, Y. Zhang, X. Cheng, Y. Li, L. Gu, K. Świerczek, High-performance anode material $Sr_2FeMo_{0.65}Ni_{0.35}O_{6-\delta}$ with in situ exsolved nanoparticle catalyst, ACS Nano 10 (2016) 8660–8669, https://doi.org/10.1021/acsnano.6b03979.

[47] S. Liu, Q. Liu, J.L. Luo, Highly stable and efficient catalyst with in situ exsolved Fe-Ni alloy nanospheres socketed on an oxygen deficient perovskite for direct CO_2 electrolysis, ACS Catal. 6 (2016) 6219–6228, https://doi.org/10.1021/ACSCATAL.6B01555.

[48] M.C. Biesinger, B.P. Payne, A.P. Grosvenor, L.W.M. Lau, A.R. Gerson, R.S.C. Smart, Resolving surface chemical states in XPS analysis of first row transition metals, oxides and hydroxides: Cr, Mn, Fe, Co and Ni, Appl. Surf. Sci. 257 (2011) 2717–2730, https://doi.org/10.1016/j.apsusc.2010.10.051.

[49] T. Yamashita, P. Hayes, Analysis of XPS spectra of Fe2+ and Fe3+ ions in oxide materials, Appl. Surf. Sci. 254 (2008) 2441–2449, https://doi.org/10.1016/J.APSUSC.2007.09.063.

[50] Y. Wan, Y. Xing, Y. Xie, N. Shi, J. Xu, C. Xia, Vanadium-doped strontium molybdate with exsolved Ni nanoparticles as anode material for solid oxide fuel cells, ACS Appl. Mater. Interfaces 11 (2019) 42271–42279, https://doi.org/10.1021/acsami.9b15584.

[51] U. Gupta, M. Yadav, B. Saini, R. Krishnapriya, R.K. Sharma, Fe_xNi_y/SiO₂-Al2O3 catalyzed hydrodeoxygenation of biorenewable platform molecules, Fuel 360 (2024) 130588, https://doi.org/10.1016/J.FUEL.2023.130588.

[52] L. Liu, S. Das, T. Chen, N. Dewangan, J. Ashok, S. Xi, A. Borgna, Z. Li, S. Kawi, Low temperature catalytic reverse water-gas shift reaction over perovskite catalysts in DBD plasma, Appl. Catal. B Environ. 265 (2020) 118573, https://doi.org/10.1016/j.apcatb.2019.118573.

[53] C.J. Fu, Q. Ma, L. Gao, S. Li, Recent advances in perovskite oxides electrocatalysts: ordered perovskites, cations segregation and exsolution, ChemCatChem 15 (2023) e202300389, https://doi.org/10.1002/CCTC.202300389.